Journal of Advances in Modeling Earth Systems

Supporting Information for

One Stomatal Model to Rule Them All? Towards Improved Representation of Carbon and Water Exchange in Global Models

Manon E.B. Sabot[1,2*], Martin G. De Kauwe[3,1,2], Andy J. Pitman[1,2], Belinda E. Medlyn[4], David Ellsworth[4], Nicolas Martin-StPaul[5], Jin Wu[6,7], Brendan Choat[4], Jean-Marc Limousin[8], Patrick J. Mitchell[9], Alistair Rogers[10], Shawn P. Serbin[10]

[1] ARC Centre of Excellence for Climate Extremes, Sydney, NSW 2052, Australia

[2] Climate Change Research Centre, University of New South Wales, Sydney, NSW 2052, Australia

[3] School of Biological Sciences, University of Bristol, 24 Tyndall Avenue, Bristol BS81TQ, United Kingdom

[4] Hawkesbury Institute for the Environment, Western Sydney University, Locked Bag 1797, Penrith, NSW 2751, Australia

[5] INRAE, URFM, Domaine Saint Paul, Centre de recherche PACA, 228 route de l'Aérodrome, CS 40509, Domaine Saint-Paul, Site Agroparc, France

[6] School of Biological Sciences, The University of Hong Kong, Pofulam, Hong Kong, China

[7] State Key Laboratory of Agrobiotechnology, The Chinese University of Hong Kong, Hong Kong, China

[8] CEFE, Univ Montpellier, CNRS, EPHE, IRD, Univ Paul Valéry Montpellier 3, Montpellier, France

[9] CSIRO Agriculture and Food, Hobart, TAS 7005, Australia

[10] Environmental and Climate Sciences Department, Brookhaven National Laboratory, Upton, NY 11973-5000, USA

Contents of this file

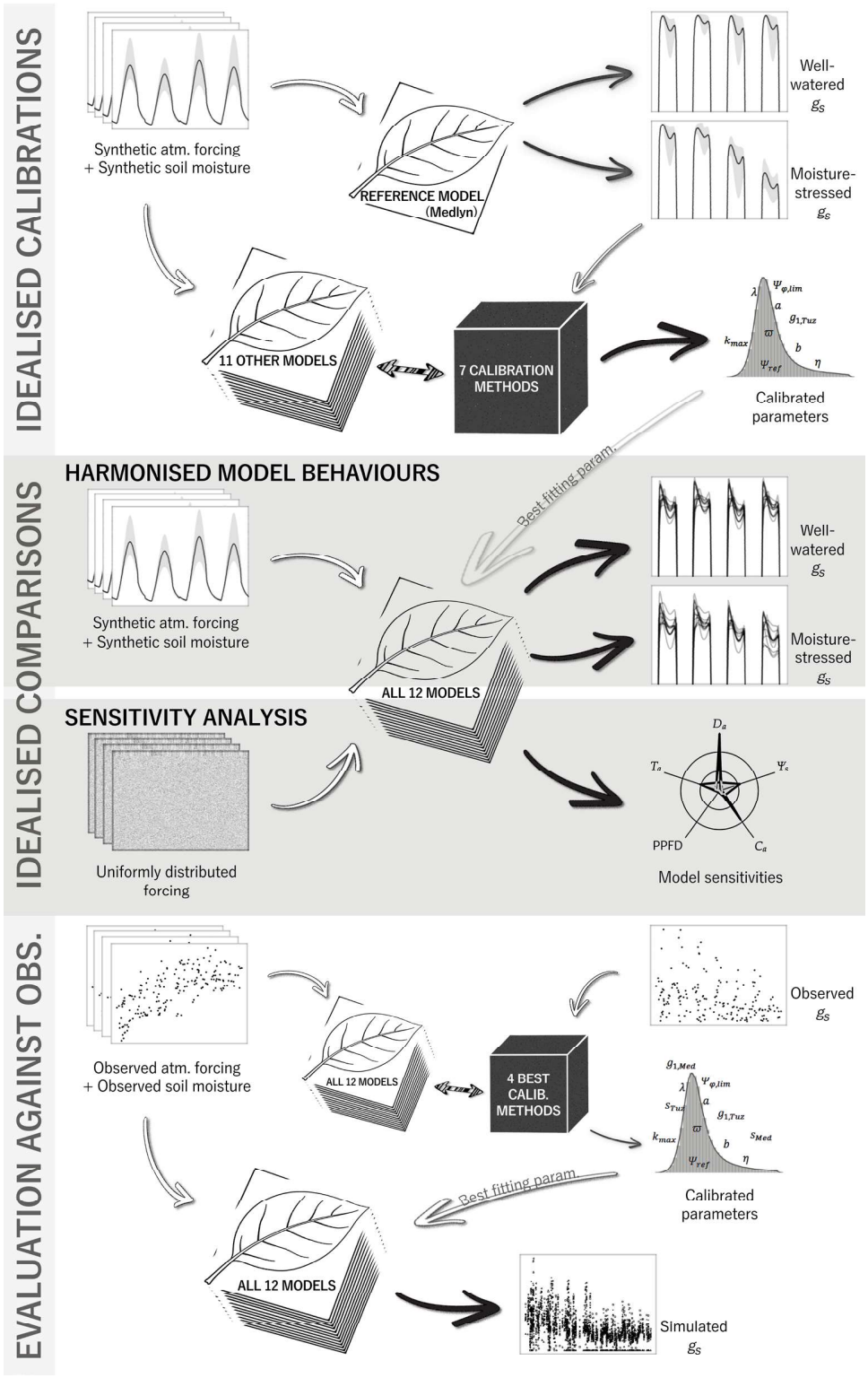

Figure S1. A schematic showing the model experiment carried out in this study, from the 'Idealised calibrations' (Methods 2.2.1), to the 'Harmonised model behaviours' (Appendix A) and 'Sensitivity analysis' (Methods 2.2.2), as well as the 'Evaluation against observations' (Methods 2.3). To ease interpretation, white arrows start from the inputs and end at the models/calibration methods, whereas black arrows start from the models/calibration methods and end at the output.

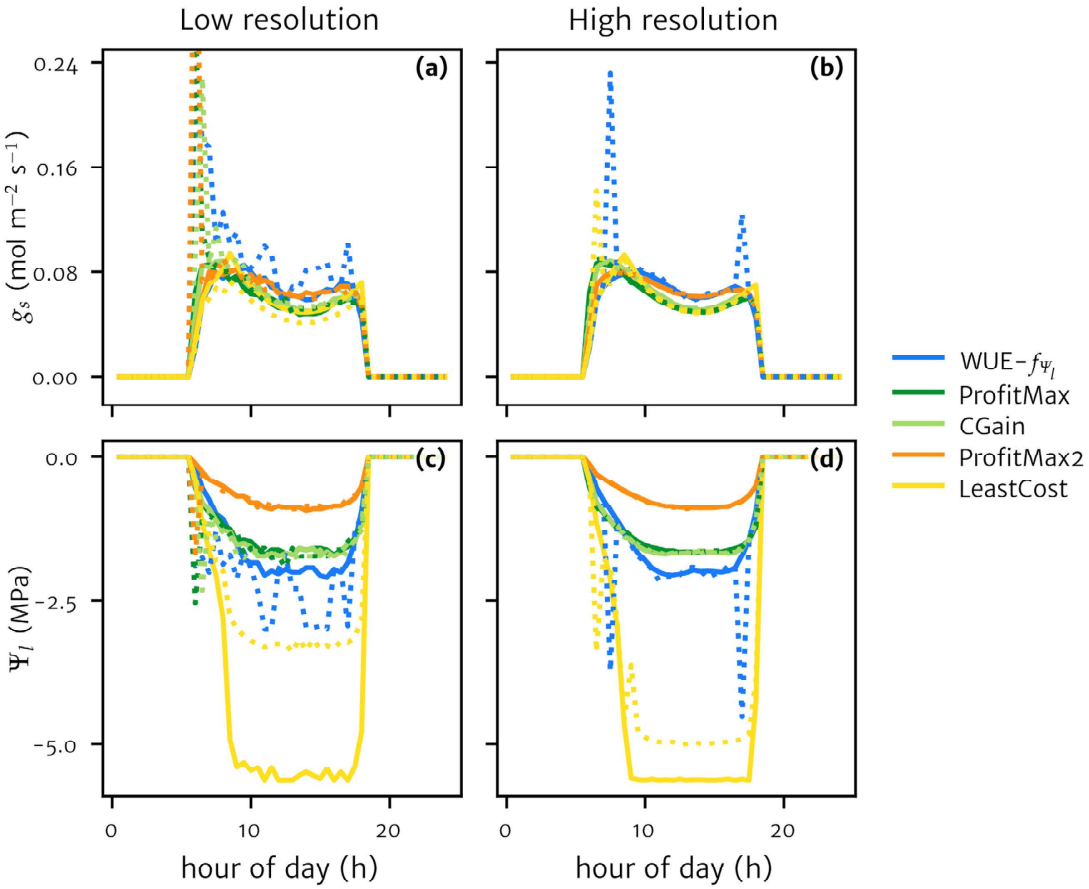

Figure S2. An example diurnal time course of stomatal conductance (g_s; panels **a** and **b**) and leaf water potential (Ψ_l; panels **c** and **d**) predicted by 5 stomatal optimisation models, depending on implementation form and solver resolution. Plain lines show the actual optimisation criteria forms and dotted lines show their commonly used derivative forms. At low resolution (panels **a** and **c**), 100,000 solutions to the optimisation problem are tested at every instant, whereas at high resolution (panels **b** and **d**) there are 4,800,000 possibilities for the optimal model to choose from in the solving matrices.

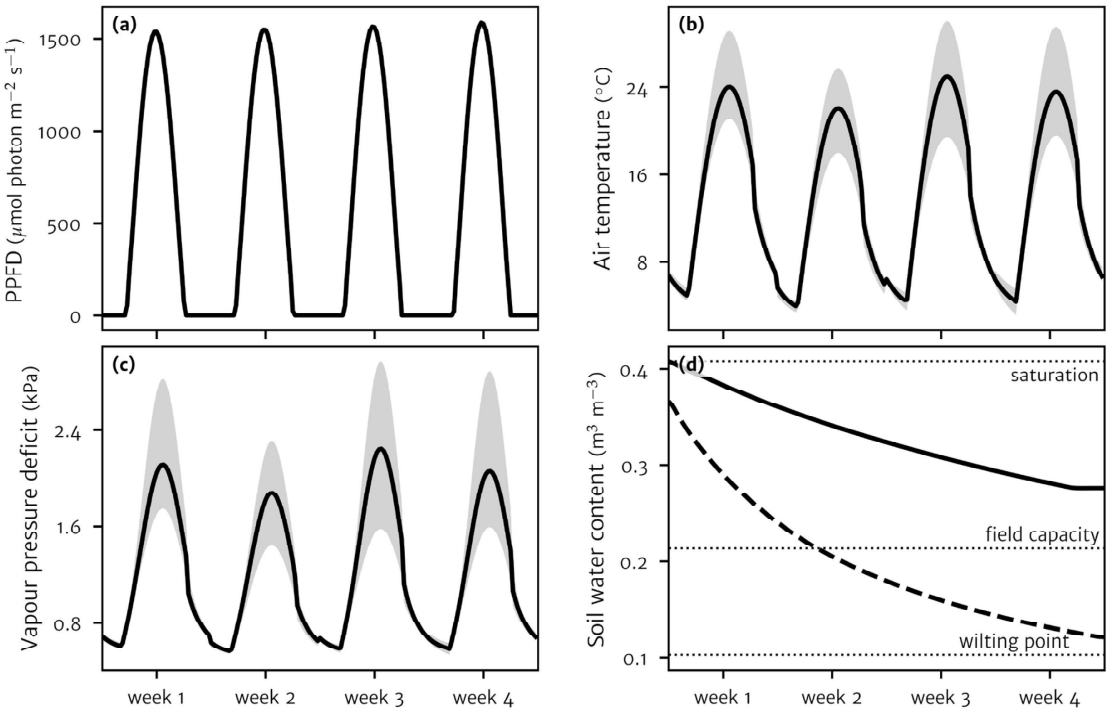

Figure S3. Synthetic half-hourly meteorological forcing (panels **a** – **c**) and soil moisture profiles (panel **d**) generated for a temperate coniferous forest (36°N, 79°W) during the northern hemisphere growing season. Black lines represent the average diurnal cycle of these variables over the course of four week and grey shadings show the minimum to maximum diurnal ranges. Meteorological drivers shown are: (**a**) the photosynthetic photon flux density (PPFD); (**b**) the air temperature; (**c**) the vapour pressure deficit. (**d**) shows the two different dry-down rates used in this study: well-watered conditions (solid line) and moderately stressed conditions (dashed line).

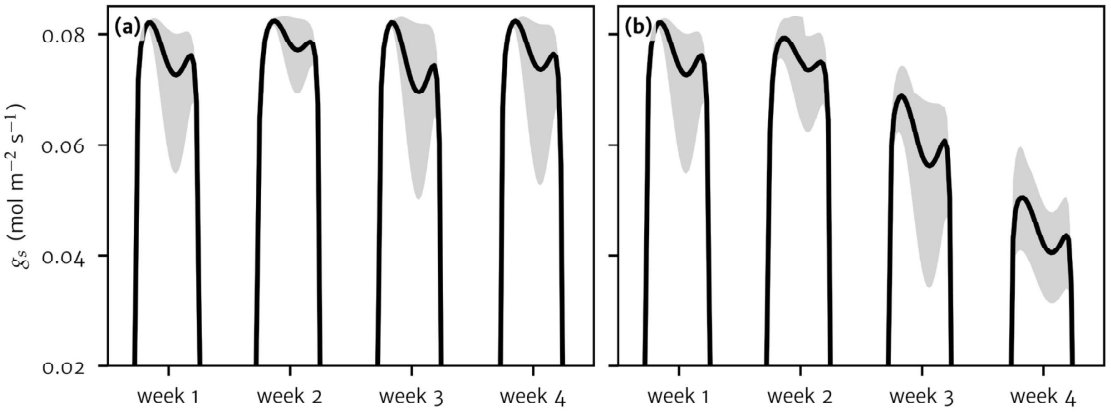

Figure S4. Reference timeseries of stomatal conductance (g_s) simulated using the Medlyn model and the atmospheric forcing from Figure S3. (**a**) shows g_s under the well-watered conditions from Figure S3d and (**b**) shows g_s undergoing the soil moisture stress. Black lines represent the average diurnal cycle of these variables over the course of four week and grey shadings show the minimum to maximum diurnal ranges.

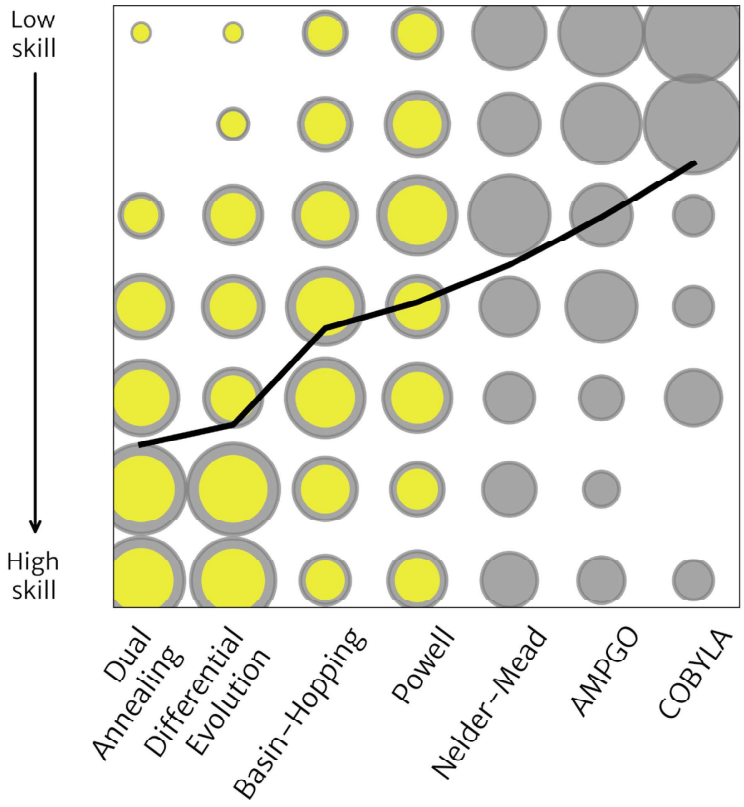

Figure S5. Ranked solver skill across models (i.e., 11 calibrated models), calibration datasets (i.e., one 4-week dataset plus three 7-day datasets), and soil moisture conditions (i.e., 'Wet' and 'Stressed'). Each solver for a given model, calibration dataset, and soil moisture type received a rank between 1 (most skilled) and 7 (least skilled). Dot size is proportional to the number of times a solver received a given rank value and, in total, each solver received 88 different ranks. The rank average for a given solver is shown in the black line. The overall most skilled solvers, that received the lowest ranks the most often, are highlighted in yellow.

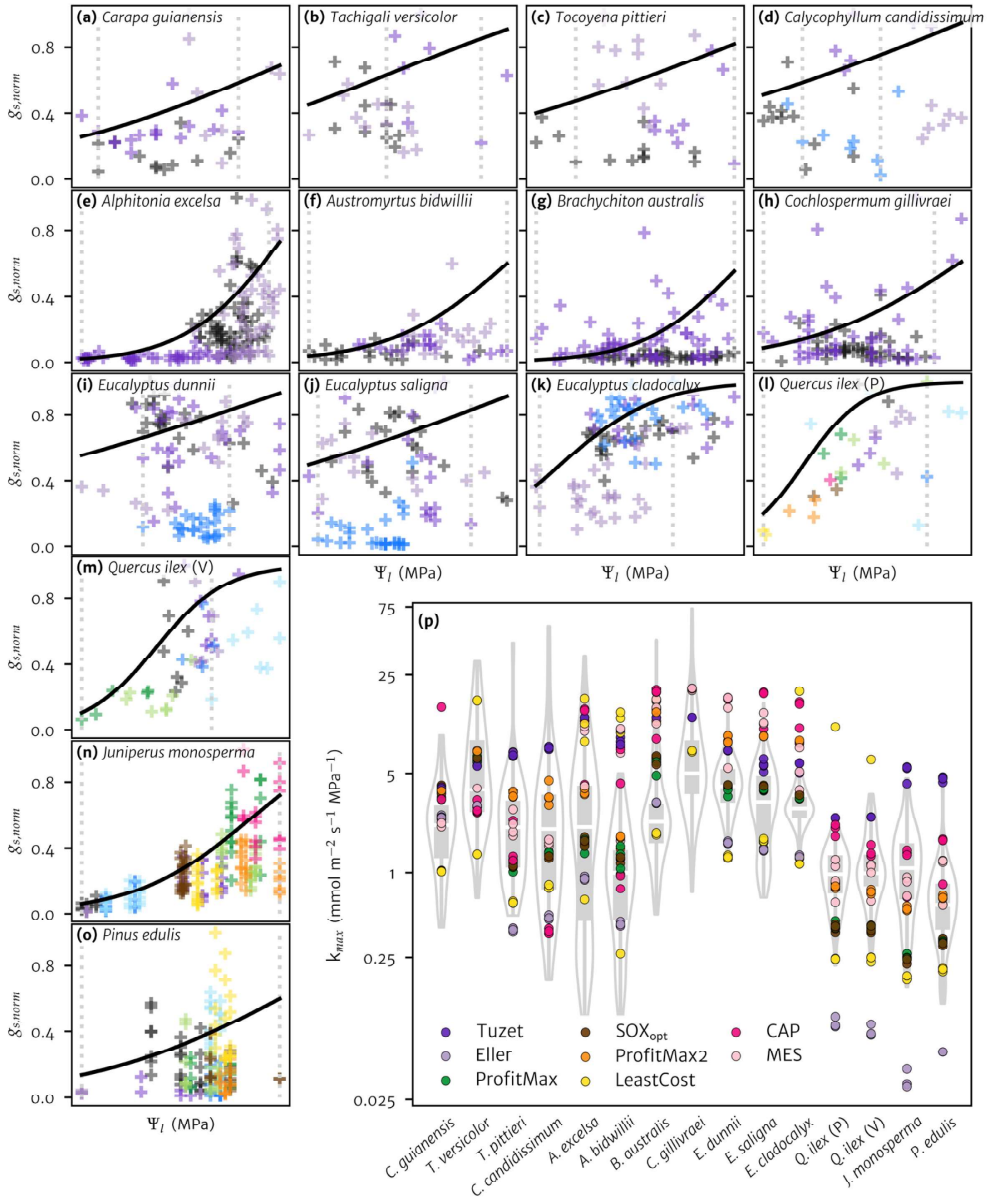

Figure S6. (**a**) – (**o**) show the observed stomatal conductance (g_s) and leaf water potential (Ψ_l) used to estimate the empirical g_s down-regulation function (ζ) of the Tuzet et al. (2003) model (see Text S6). These panels are intended to illustrate the challenge of estimating ζ, so the ranges of Ψ_l – which vary between -0.4 to -3.7 MPa and -1.7 to -5.8 MPa – are not shown, keeping the figure readable. The dashed vertical lines correspond to the first inflexion point between g_s and Ψ_l and to the inflexion point associated with the smallest g_s to Ψ_l association. The black lines show the fitted ζ functions. In each case, g_s was normalised by the maximum observed value. Within each subplot, colours mark the different calendar days at which the data were measured. (**p**) shows all calibrated maximum hydraulic conductance (k_{max}) parameters per model and site × species (i.e., using the four overall most skilled solvers highlighted in Figure S5). The violin plots show the maximum conductance obtained from all the observed transpiration (E), Ψ_l, and soil water potential (Ψ_s), using $k_{max} = E / \int_{\Psi_s}^{\Psi_l} VC \, d\Psi$ where VC is the parameterised plant vulnerability curve. Light grey boxes within the violin plots show the interquartile ranges, with the median marked by a white horizontal line. Site × species appear from wet (left hand side) to xeric (right hand side).

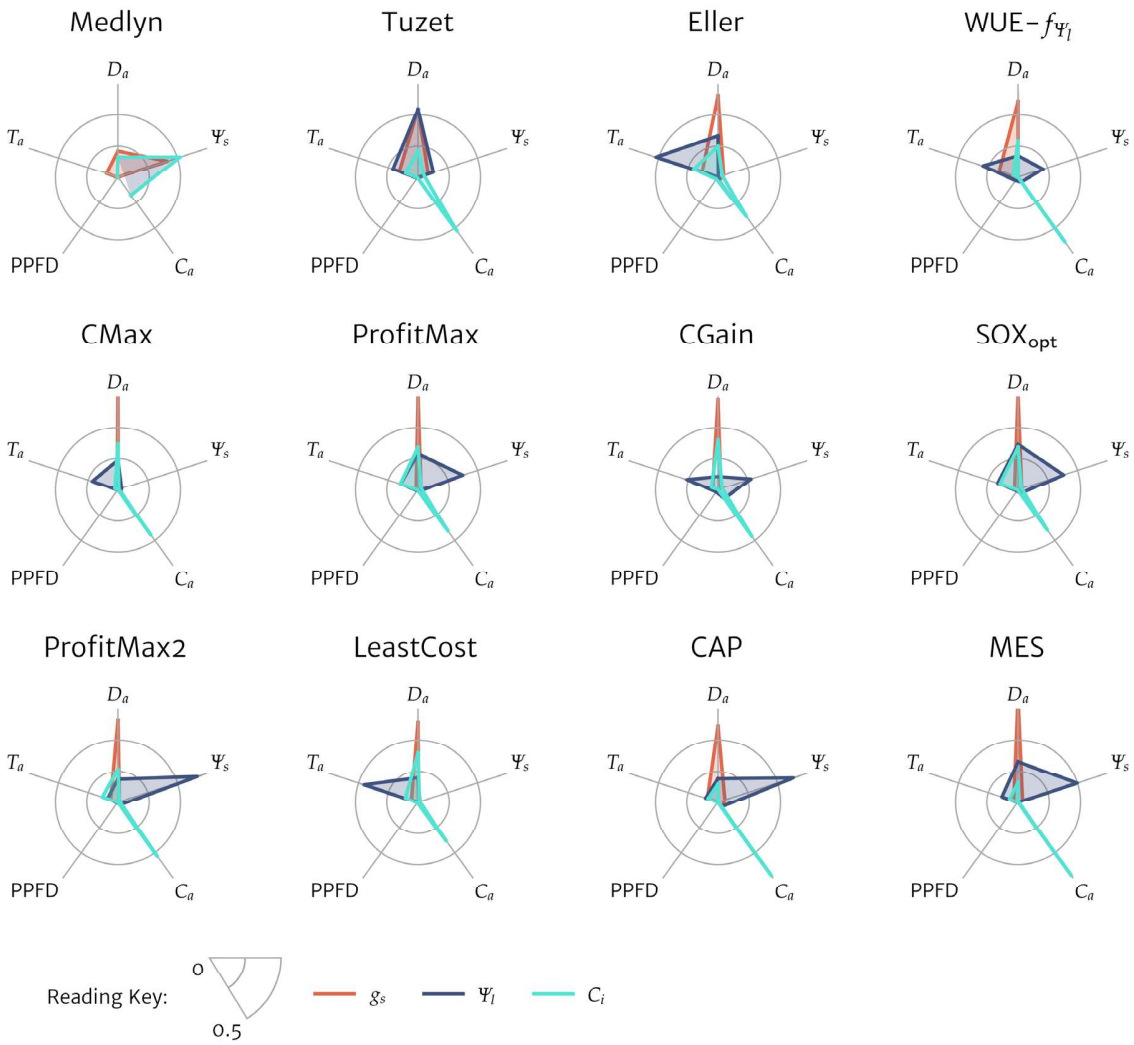

Figure S7. First-order Sobol' sensitivity indices of the stomatal conductance (g_s), leaf water potential (Ψ_l), and CO_2 concentration in the leaf intercellular air spaces (C_i) to variability in environmental drivers for the 12 models parameterised under well-watered conditions. Environmental drivers are: (i) atmospheric vapour pressure deficit (D_a); (ii) soil water potential (Ψ_s); (iii) ambient CO_2 concentration (C_a); (iv) photosynthetic photon flux density (PPFD); and (v) air temperature (T_a). The concentric circles mark 0.25 increments on a scale of 0 to 0.5, with 0 signifying no influence and 0.5 high influence.

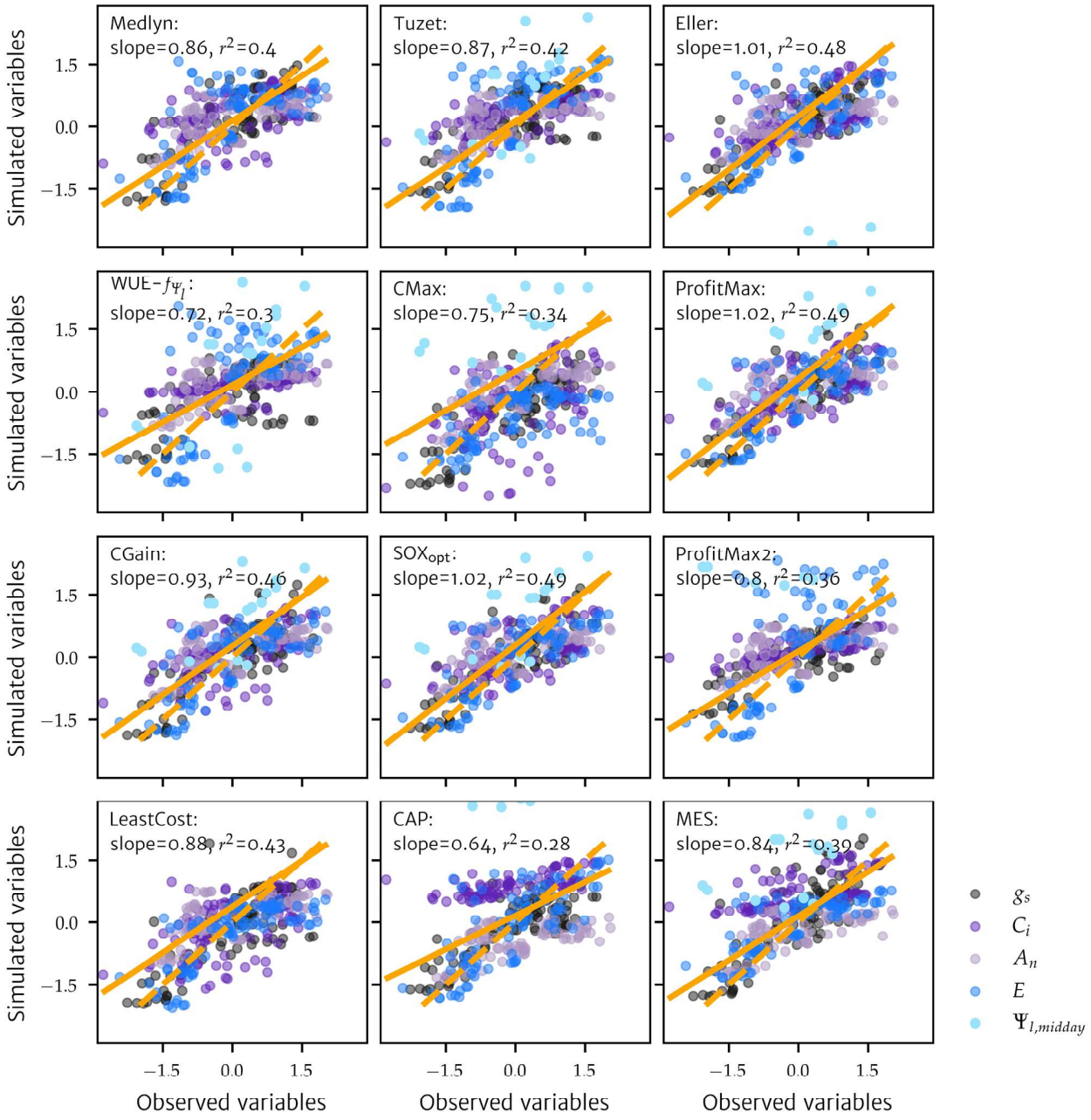

Figure S8. Studentised (each value minus the observed average, normalised by the observed standard deviation) observed to modelled measures of output variables for *Eucalyptus cladocalyx* for the twelve models compared. The variables shown are stomatal conductance (g_s), intercellular CO_2 concentration (C_i), transpiration (E), net CO_2 assimilation (A_n), and midday leaf water potential ($\Psi_{l,midday}$). The 1:1 line appears in the dashed orange, and the solid line is the overall regression for the g_s, C_i, E, and A_n outputs (n=450, p<0.001, with the slope and r^2 shown after each model name). For fairness, $\Psi_{l,midday}$ is not used to estimate the regressions and r^2 because the Medlyn model does not predict leaf water potential.

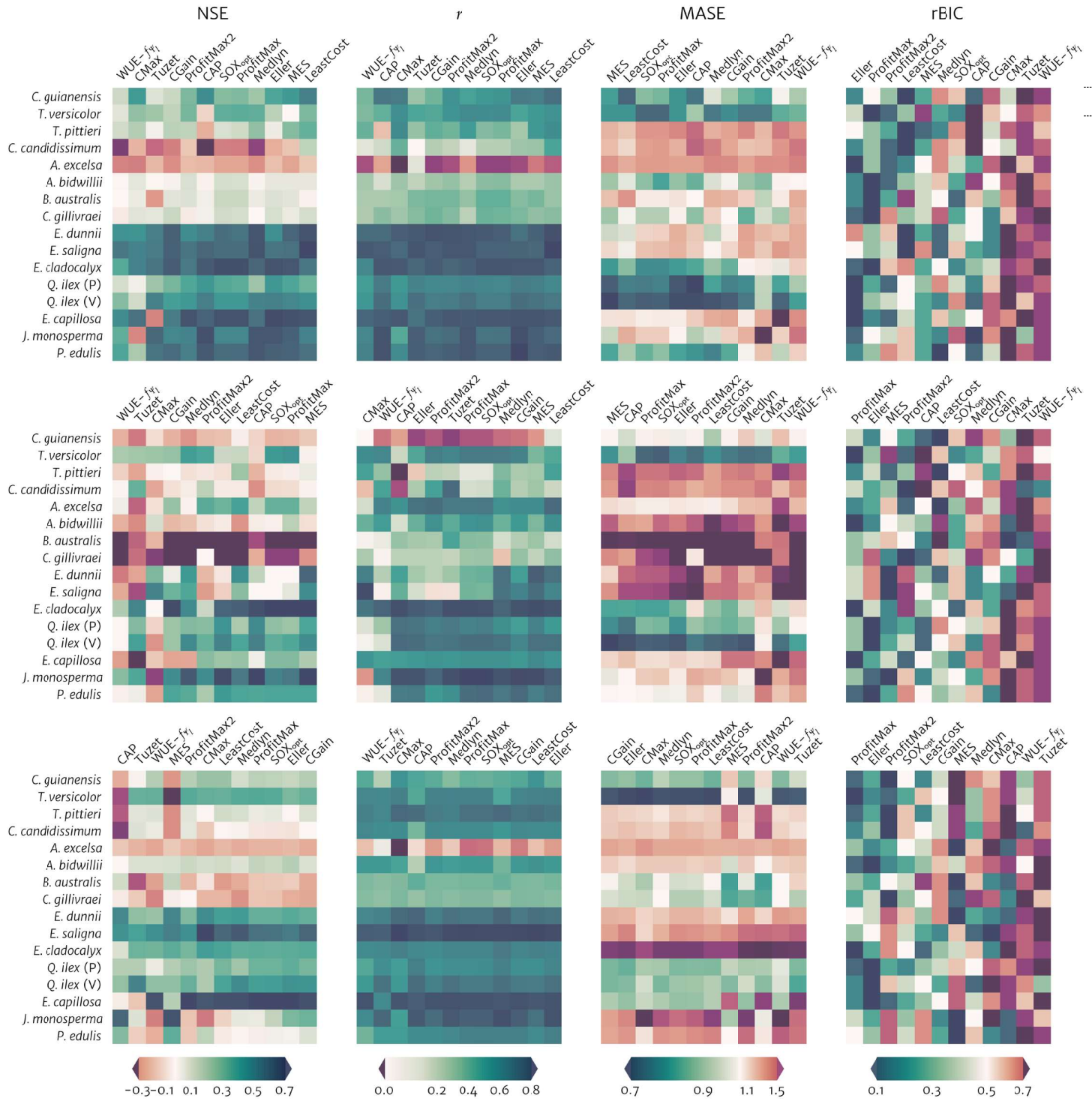

(a)	**(b)**	**(c)**	**(d)**
(e)	**(f)**	**(g)**	**(h)**
(i)	**(j)**	**(k)**	**(l)**

Figure S9. Nash-Sutcliffe Efficiency index (NSE; panels **a**, **e**, **i**); Pearson's correlation coefficient (r; panels **b**, **f**, **j**); Mean Absolute Scaled Error (MASE; panels **c**, **g**, **k**); and ranked Bayesian Information Criteria (rBIC; panels **d**, **h**, **l**) for the 12 models' stomatal conductance (panels **a** – **d**), transpiration (panels **e** – **h**), and net photosynthetic uptake (panels **i** – **l**) estimates across sites × species. For the NSE and r, from left to right, the models appear in order of least to most skilled across sites × species for a given leaf-level flux; a score of 1 characterises a perfect forecast. For the MASE and rBIC, the models appear in order of most to least skilled; scores of 0 characterise best possible and perfect forecasts, respectively.

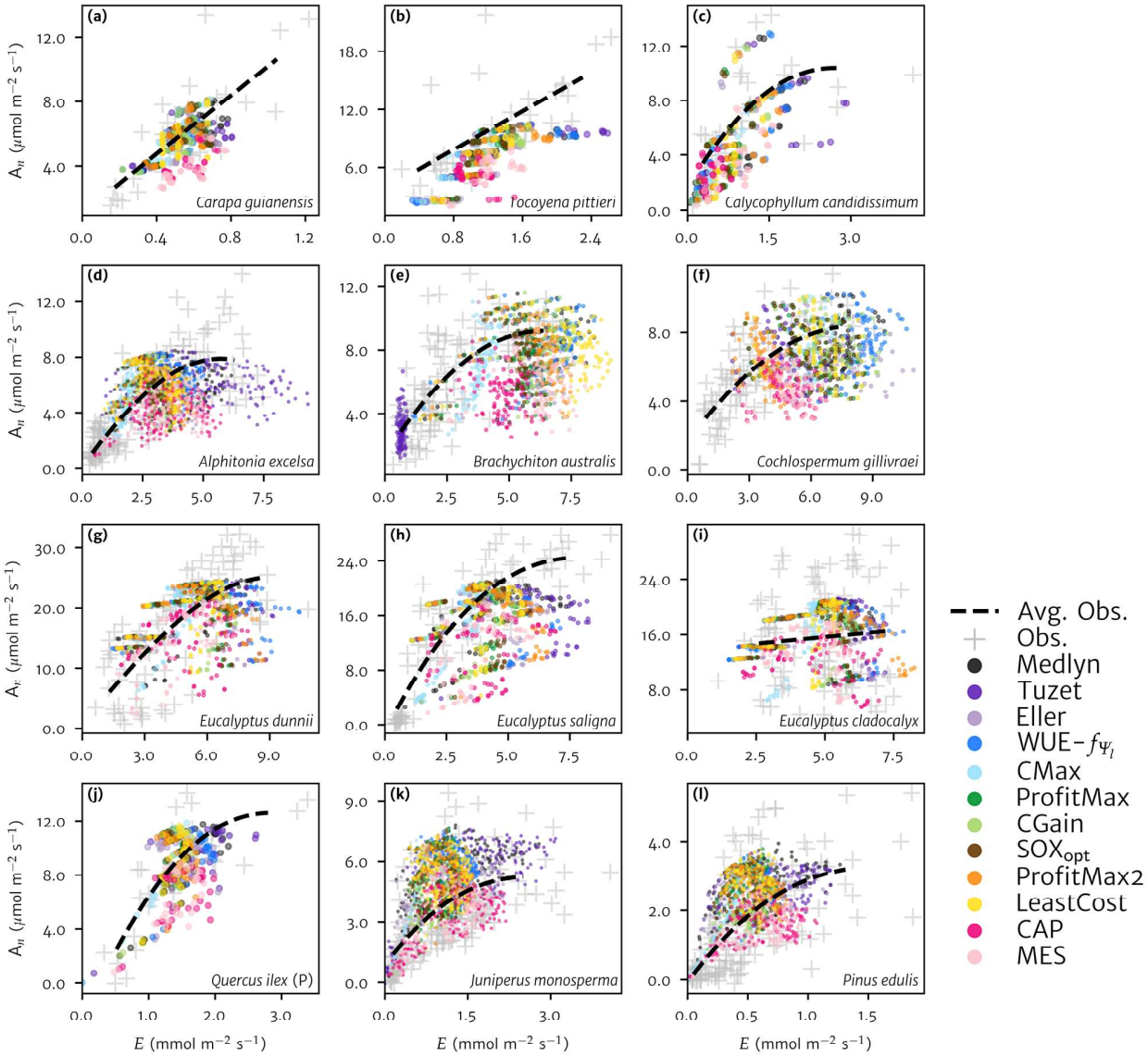

Figure S10. Leaf-level estimates of the net rates of carbon assimilation (A_n) and transpiration (E) for the 12 models at the site × species not shown in Figure 6, from wet (panel **a**) to xeric (panel **d**), compared to observations (light grey crosses). Dashed black lines represent the observed overall average behaviours fitted via a generalised additive model. For the model estimates, point size is proportional to the number of observations per site × species and transparency is proportional to density. Outliers were excluded by capping the modelled values to 2.5 times the maximum observation at each site.

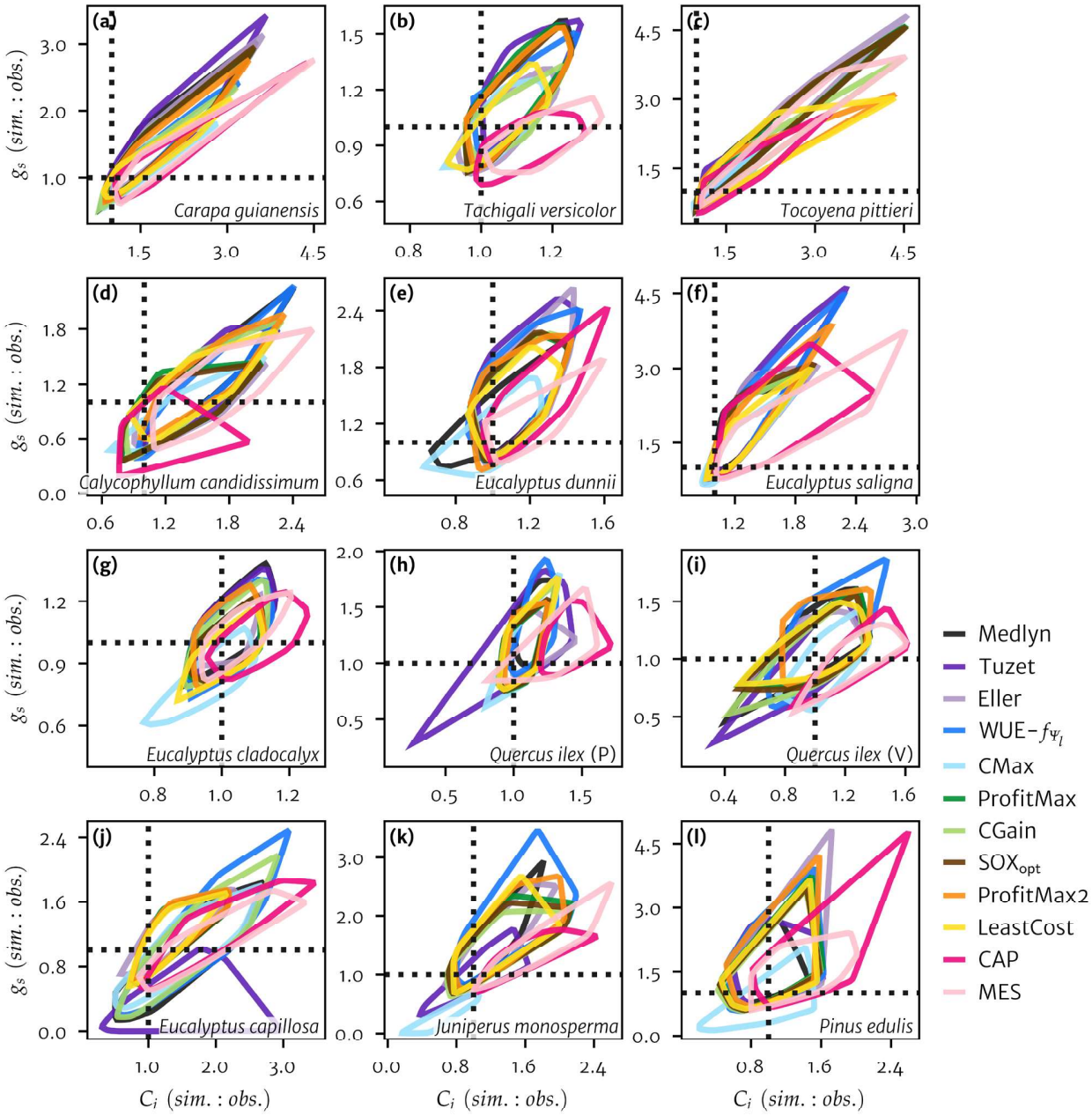

Figure S11. Relationship between stomatal conductance (g_s) and the CO_2 concentration in the leaf intercellular air spaces (C_i) predicted by the 12 models for wet (panel **a**) to xeric (panel **k**) site × species. The encircles show the interquartile ranges of simulated to observed g_s ratios against simulated to observed C_i ratios, such that a perfect model would be concentrated at the intersection of the 1:1 lines.

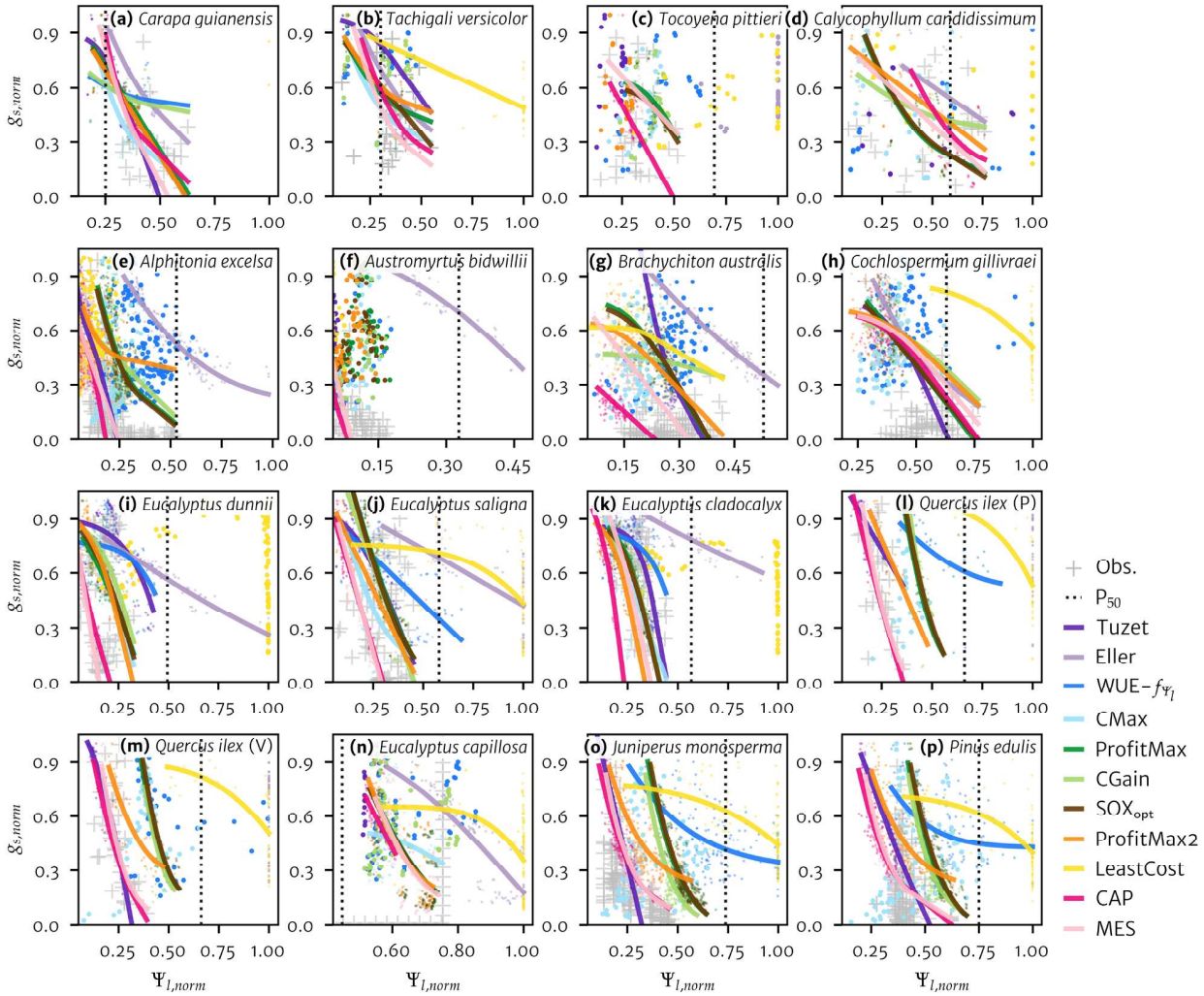

Figure S12. Relationship between stomatal conductance (g_s) and leaf water potential (Ψ_l) predicted by 11 models for wet (panel **a**) to xeric (panel **p**) site × species. The decline in g_s with decreasing Ψ_l is fitted via a generalised additive model and compared to observations (light grey crosses). The functional forms were made comparable by normalising g_s by its model-specific maximum for each site × species, and Ψ_l by the critical leaf water potential indicative of total xylem failure (P_{95} in this study). Curves were not fitted if they did not monotonically decrease, or where the models operate at, or beyond, the P_{95}. Note, there are no observations available for (**n**), so we plotted the measured minimum average seasonal Ψ_l and the minimum observed g_s instead.

Table S1. Default parameters of the biochemical photosynthesis model

Abbreviation	Parameter description	Value	Unit
O_a	atmospheric O_2 concentration	20.73	kPa
Γ^*_{25}	CO_2 compensation point at 25°C	4.22	Pa
K_c	Michaelis-Menten constant for carboxylation	39.96	Pa
K_o	Michaelis-Menten constant for oxygenation	27.48	kPa
E_c	energy of activation of the carboxylation	79430	J mol^{-1}
E_o	energy of activation of the oxygenation	36380	J mol^{-1}
E_v	energy of activation of V_{cmax}	60000	J mol^{-1}
E_j	energy of activation of J_{max}	30000	J mol^{-1}
E_{Γ^*}	energy of activation of the CO_2 compensation point	37830	J mol^{-1}
δ_{S_v}	V_{cmax} entropy factor	650	J mol^{-1} K^{-1}
δ_{S_j}	J_{max} entropy factor	650	J mol^{-1} K^{-1}
H_{δ_v}	V_{cmax} rate of decrease above the optimum temperature	200000	J mol^{-1}
H_{δ_j}	J_{max} rate of decrease above the optimum temperature	200000	J mol^{-1}
τ_l	short wave (visible) leaf transmittivity	0.05	-
α_l	short wave (visible) leaf reflectivity	0.062	-
α	quantum yield of electron transport	0.30	mol photon mol^{-1} electron
c	curvature of the light response	0.7	-
h	transition curvature factor	0.99	-

Table S2. Default soil parameters

Abbreviation	Parameter description	Value	Unit
Ψ_{aep}	air entry point soil water potential	-0.8	kPa
θ_{sat}	volumetric soil water content at saturation	0.41	$m^3\ m^{-3}$
θ_{fc}	volumetric soil water content at field capacity	0.21	$m^3\ m^{-3}$
θ_{wp}	volumetric soil water content at wilting point	0.10	$m^3\ m^{-3}$
b_{CH}	Clapp-Hornberger pore size distribution index	5.22	-

Table S3. Sampled parameter spaces for each stomatal conductance model

Model name	Parameter	Unit	Initial guess***	Sampled parameter space
Medlyn	$g_{1,Med}$	$kPa^{0.5}$	2.49	[0.01; 12.5]
	s_{Med}	MPa^{-1}	2	[0.01; 10]
Tuzet	k_{max}*	mmol m^{-2} s^{-1} MPa^{-1}	1	[0.005; 20]
	$g_{1,Tuz}$	–	3.5	[0.01; 12.5]
	Ψ_{ref}**	MPa	P_{50} (P_{88})****	[P_{95}; -0.15]
Eller	k_{max}	mmol m^{-2} s^{-1} MPa^{-1}	1	[0.005; 20]
WUE-f_{Ψ_l}	λ	µmol CO_2 $mmol^{-1}$ H_2O	5	[0.01; 10] × 10^3
CMax	a	µmol m^{-2} s^{-1} MPa^{-2}	5	[0.5 ; 80]
	b	µmol m^{-2} s^{-1} MPa^{-1}	-1	[-8 ; -0.1]
ProfitMax	k_{max}	mmol m^{-2} s^{-1} MPa^{-1}	1	[0.005; 20]
CGain	ϖ	µmol m^{-2} s^{-1}	5	[0.01 ; 50]
SOX_{opt}	k_{max}	mmol m^{-2} s^{-1} MPa^{-1}	1	[0.005; 20]
ProfitMax2	k_{max}	mmol m^{-2} s^{-1} MPa^{-1}	1	[0.005; 20]
LeastCost	k_{max}	mmol m^{-2} s^{-1} MPa^{-1}	1	[0.005; 20]
	η	µmol CO_2 $mmol^{-1}$ H_2O	5	[0.01 ; 50] × 10^3
CAP	k_{max}	mmol m^{-2} s^{-1} MPa^{-1}	1	[0.005; 20]
	$\Psi_{\varphi,lim}$	MPa	P_{50} (P_{88})****	[P_{95}; -0.15]
MES	k_{max}	mmol m^{-2} s^{-1} MPa^{-1}	1	[0.005; 20]
	$\Psi_{\varphi,lim}$	MPa	P_{50} (P_{88})****	[P_{95}; -0.15]

* Calibrations performed in the 'Evaluation against observations' section only
** Parameter calibrated in the theoretical 'Idealised calibrations' section but see Methods S5 for the 'Evaluation against observations' section
*** The initial value was multiplied by 1.5 in case of calibration failure (this happened once, for one model at one site × species combination in the 'Evaluation against observations'; see output data)
**** P_{50} is replaced by P_{88} if the initial $\Psi_s < P_{50}$

Table S4. Overview of the minimisers used in this study

	Solver description	**Suited to…**	**Reference**
Nelder-Mead	Simplex search algorithm	Unimodal problems	Nelder & Mead (1965)
COBYLA	Simplex polynomial search algorithm	Constrained complex problems	Powell (1994)
Powell	Conjugate direction algorithm	Continuous complex problems	Powell (1964)
Differential Evolution	Stochastic population algorithm	Global problems	Storn & Price (1997)
Dual Annealing	Simulated annealing algorithm with stochastic sampling	Global problems	Xiang & Gong (2000)
AMPGO	Adaptive memory programming algorithm	Constrained global problems	Lasdon et al. (2010)
Basin-Hopping	Two-phase stochastic algorithm	Global problems	Wales & Doye (1997)

Table S5. Species-level parameterisations of the canopy

Species		**Height*** **(m)**	**Reference**	α_l **(-)**
C. guianensis		33.9	Wu et al. (2020)	0.2
T. versicolor		30.4		0.2
T. pittieri		26.6		0.2
C. candidissimum		20.1		0.2
A. excelsa		20**		0.15
A. bidwillii		5**		0.15
B. australis		20**		0.15
C. gillivraei		20**		0.15
E. cladocalyx		6.1	Héroult et al. (2013)	0.15
E. dunnii		8.8		0.15
E. saligna		8.3		0.15
E. capillosa		13	Mitchell et al. (2009)	0.15
J. monosperma		3.5	Limousin et al. (2013)	0.05
P. edulis		3.5		0.05
Q. ilex	Vic la Gardiole	5.5	Martin-StPaul et al. (2012)	0.15
	Puéchabon	6.5		

** Height is only used by the Eller model

** Heights are not given in Choat et al. (2006), so we use the model's default value of 20 m for upper canopy species and 5 m for understorey species

Table S6. Best parameter values from the idealised calibrations. Associated minimisers are shown inside the brackets.

Model name	Parameter	Unit	'Wet' soil moisture profile		'Stressed' soil moisture profile	
Tuzet	$g_{1,Tuz}$	–	3.32	(Powell)	3.05	(Dual Annealing)
	Ψ_{ref}	MPa	-2.52		-2.23	
Eller	k_{max}	mmol m^{-2} s^{-1} MPa^{-1}	0.32	(Powell)	0.26	(Powell)
WUE-f_{Ψ_l}	λ	µmol CO_2 $mmol^{-1}$ H_2O	1.34	(Dual Annealing)	1.82	(Dual Annealing)
CMax	a	µmol m^{-2} s^{-1} MPa^{-2}	2.26	(Dual Annealing)	2.44	(Dual Annealing)
	b	µmol m^{-2} s^{-1} MPa^{-1}	-2.69		-1.80	
ProfitMax	k_{max}	mmol m^{-2} s^{-1} MPa^{-1}	0.89	(Basin-Hopping)	0.78	(Basin-Hopping)
CGain	ϖ	µmol m^{-2} s^{-1}	7.24	(Dual Annealing)	8.07	(Dual Annealing)
SOX_{opt}	k_{max}	mmol m^{-2} s^{-1} MPa^{-1}	0.87	(Powell)	0.76	(Dual Annealing)
ProfitMax2	k_{max}	mmol m^{-2} s^{-1} MPa^{-1}	1.99	(Nelder-Mead)	1.53	(Nelder-Mead)
LeastCost	k_{max}	mmol m^{-2} s^{-1} MPa^{-1}	0.44	(Differential Evolution)	0.37	(Dual Annealing)
	η	µmol CO_2 $mmol^{-1}$ H_2O	3.50		4.79	
CAP	k_{max}	mmol m^{-2} s^{-1} MPa^{-1}	1.98	(Basin-Hopping)	6.23	(Dual Annealing)
	$\Psi_{\varphi,lim}$	MPa	-3.15		-0.89	
MES	k_{max}	mmol m^{-2} s^{-1} MPa^{-1}	1.19	(Dual Annealing)	3.94	(Differential Evolution)
	$\Psi_{\varphi,lim}$	MPa	-3.27		-0.90	

Text S1. Biochemical photosynthesis model

The net rate of carbon assimilation, A_n (µmol m^{-2} s^{-1}), is obtained from the Farquhar et al. (1980) biochemical photosynthesis model, including the Rubisco limited photosynthetic rate (A_c; µmol m^{-2} s^{-1}) and the rubilose-1,5-bisphosphate (RuBP) regeneration limited rate (A_j; µmol m^{-2} s^{-1}), with a smoothed hyperbolic transition between these two limitations (Kirschbaum & Farquhar, 1984).

$$A_n = \frac{A_c + A_j - \sqrt{(A_c + A_j)^2 - 4\,h\,A_c\,A_j}}{2\,h} - R_d \qquad (1.1)$$

where h is a unitless transition curvature factor and R_d (µmol m^{-2} s^{-1}) is the day respiration, taken as 1.5% of the photosynthetic Rubisco capacity, V_{cmax} (µmol m^{-2} s^{-1}), as per Collatz et al. (1991).

The expressions of the Rubisco limited rate, A_c (µmol m^{-2} s^{-1}), and of the electron transport limited rate were obtained from De Pury & Farquhar (1997):

$$A_c = \frac{V_{cmax}(C_i - \Gamma^*)}{C_i + K_m} \qquad (1.2)$$

where C_i (Pa) is the intercellular CO_2 partial pressure, Γ^* (Pa) is the CO_2 compensation point of photosynthesis. K_m (Pa) is the effective Michaelis-Menten constant:

$$K_m = K_c\left(1 + \frac{O_a}{K_o}\right) \qquad (1.3)$$

where K_c (Pa) is the Michaelis-Menten constant of Rubisco for CO_2, K_o (Pa) the Michaelis-Menten constant of Rubisco for O_2, and O_a (Pa) is the atmospheric oxygen partial pressure.

The second limitation, A_j (µmol m^{-2} s^{-1}), is expressed as:

$$A_j = \frac{J\,(C_i - \Gamma^*)}{4\,(C_i + 2\Gamma^*)} \qquad (1.4)$$

where J (µmol m^{-2} s^{-1}) is the irradiance dependence of electron transport, such that:

$$J = \frac{\alpha PPFD + J_{max} - \sqrt{(\alpha PPFD + J_{max})^2 - 4c\alpha J_{max} PPFD}}{2c} \qquad (1.5)$$

where α (mol photon mol^{-1} electron) is the effective quantum yield of electron transport depending on leaf emissivity, $PPFD$ (µmol m^{-2} s^{-1}) is the photosynthetic photon flux density, J_{max} (µmol m^{-2} s^{-1}) is the maximum rate of electron transport, and c defines the unitless curvature of the leaf response of electron transport to irradiance.

The temperature dependency of Γ^*, K_c, and K_o is modelled using an Arrhenius function relative to 25 °C, as in De Pury & Farquhar (1997).

The temperature dependency of V_{cmax} and J_{max} is modelled using a peaked Arrhenius function relative to 25 °C, to account for limitations at high temperature, as in Medlyn et al. (2002). To account for low temperatures effects (i.e., below 10°C), we simply apply a linear ramp.

Text S2. Shape of the vulnerability curves

The sensitivity (s_1, MPa) and shape (s_2, unitless) parameters used to model the cumulative Weibull distribution (Neufeld et al., 1992) were derived from two values of water potential drop in xylem hydraulic conductivity, such that:

$$s_2 = \frac{\log\left(\frac{\log\left(1 - {x_1}/{100}\right)}{\log\left(1 - {x_2}/{100}\right)}\right)}{\log P_{x_1} - \log P_{x_2}} \qquad (2.1)$$

$$s_1 = \frac{P_{x_1}}{(-\log(1-{}^{x_1}/_{100}))^{\frac{1}{s_2}}} \quad (2.2)$$

where x_1 and x_2 are two percentage values of hydraulic conductivity loss (%), and P_{x_1} and P_{x_2} are their associated water potentials (MPa), e.g., P_{50} and P_{88}.

Text S3. Soil hydraulic processes

Soil water potential is given by the Clapp-Hornberger equation (Clapp & Hornberger, 1978):

$$\Psi_s = \Psi_{aep} \left(\frac{\theta}{\theta_{sat}}\right)^{-b_{CH}} \quad (3.1)$$

where Ψ_s (MPa) is the root zone soil water potential, Ψ_{aep} (MPa) is the air entry point water potential, θ ($m^3\ m^{-3}$) is volumetric soil moisture content, θ_{sat} ($m^3\ m^{-3}$) is the volumetric soil moisture content at saturation, and b_{CH} (unitless) is the Clapp-Hornberger pore size distribution index which approximates the slope of the soil-water retention curve.

Text S4. Simplification of the CGain hypothesis

The optimisation hypothesis presented by Lu et al. (2020) maximises plant net carbon gain (CGain) whilst accounting for a 'carbon cost per recovered unit of xylem conductance' (ϖ; μmol $m^{-2}\ s^{-1}$):

$$\max\left(A - \varpi \frac{k\psi_{sat} - k\psi_{crit} - r_\varpi\left(k\psi_l - k\psi_{crit}\right)}{k_{max}}\right) \quad (4.1)$$

where r_ϖ sets the ratio of impaired to recovered xylem conductance after embolism and $k_{\Psi_{sat}}$ (mmol $m^{-2}\ s^{-1}\ MPa^{-1}$) corresponds to minimum embolism when soil water potential is at saturation (i.e. Ψ_{aep}).

Assuming instantaneously reversible embolism (i.e. $r_{\varpi} = 1$) is necessary to allow comparison of the CGain hypothesis with other hypotheses that do not mechanistically account for lagged costs, therefore the maximisation criterion becomes:

$$\max \left(A - \varpi \frac{k\Psi_{sat} - k\Psi_l}{k_{max}} \right) \qquad (4.2)$$

Finally, we assume no *a priori* embolism (i.e. impaired xylem perfectly and fully recovers), such that $k_{\Psi_{sat}} \sim k_{max}$ and Equation S4.2 becomes:

$$\max \left(A - \varpi \frac{k_{max} - k\Psi_l}{k_{max}} \right) \qquad (4.3)$$

Text S5. Processing of the observations and additional data

Essential hydraulic and photosynthetic parameters

For every dataset considered in this study, we discarded species for which hydraulic traits were not readily available from the literature (two Australian species) or, in the case of the Panamean species, we discarded four species for which we could not reliably reconstruct hydraulic vulnerability curves using observed P_{50} and the Weibull parameters published in Wu et al. (2020) (i.e. P_{88} within less than 1 MPa of the P_{50}), nor had access to alternative published hydraulic trait parameterisations.

Where A-C_i curves were available, we fitted $V_{cmax,25}$ and $J_{max,25}$ parameters on a site × species basis, using the Levenberg–Marquardt least-squares approach for which the source code is freely available from GitHub (https://github.com/mdekauwe/FitFarquharModel; De Kauwe et al., 2015). The fitting method makes no assumption about the C_i value at which the leaf transitions between A_c and A_j, but it uses a hyperbolic minimum function to smooth the transition (cf. Equation S1.1).

For robust estimation, we screened the data and excluded 'bad' measurement curves, with 'bad' defined according to the following criteria: (i) if the ratio of measurements in

the A_j vs. A_c part of the curve was under 3:10 or *vice versa*, (ii) if the curve comprised less than six measurements; (iii) if the fitted function $r^2 < 0.9$, and (iv) if there were anomalously large residuals, or if residuals in one part of the curve were significantly greater than those of the other part of the curve. For one Panamean species (*Carapa guianensis*), we had to relax criteria (i), as there were too few A-C_i curves, but we nonetheless excluded one curve that did not include any data in the A_c portion.

Gas exchange datasets

Measurements obtained under a PPFD threshold of 50 µmol m^{-2} s^{-1} and a D_a threshold of 0.05 kPa were filtered out. Any negative g_s, E, and C_i observations, or null g_s associated to positive A_n and E, as well as measurements of $C_i > C_a$ were removed. Only species with at least 30 observations remaining after these filtering steps were considered in the study (i.e. discarding seven species from Panama and one location from France).

Where the g_b set by the LI-COR was not available (the Many Peaks Range, Sevilleta, Puéchabon, and Vic la Gardiole), we assumed it to be 5 mol m^{-2} s^{-1} for the gymnosperm species (based on the LI-COR fixed value for conifers; https://www.licor.com/documents/vtlsnaiycs2izvrcsnu1) and 2.84 mol m^{-2} s^{-1} for the angiosperm species (following the majority of angiosperm datasets where g_b was available).

Where atmospheric measurements of T_a, D_a, or P_{atm} were missing, we proceeded in two different ways. Firstly, if either T_a or D_a or P_{atm} was missing whilst the two other variables were reported, we gap-filled the missing variable using Teten's equation (Monteith & Unsworth, 1990) and depending on site elevation. Secondly, where two or more of the above atmospheric data were not available (i.e. at the Many Peaks Range, QLD, Australia and Sevilleta, NM, USA), we added the closest corresponding observations (matched to the nearest half hour) from the nearest weather station.
For the Many Peaks Range, the weather data were obtained from the Australian Government's Bureau of Meteorology archive for the Townsville Aero station,

approximately 105 km away from where the leaf-gas exchange measurements were made. The temperature data diverged from the measured leaf temperatures by up to >10°C, so we bias corrected them using the midway points between air and leaf temperatures. For Sevilleta, the weather data were obtained from a micrometeorological station located in an open inter-canopy area at the study site (see https://sevlter.unm.edu/data/sev-273).

In all cases, whenever added atmospheric forcing violated Tetens' equation (i.e., T_a, D_a, and P_{atm} corresponding to >95% relative humidity but not immediately preceded or succeeded by relative humidity >90%), we removed that data.

Text S6. Fitting the Tuzet model's ζ function

For each site × species, we smoothed the normalised observations of g_s (normalised by the maximum observed value) using a gaussian filter. We then determined the first inflexion point (x_0) in the smoothed $g_{s,norm}$ to observed Ψ_l relationship, and a i^{th} inflexion point (x_i) corresponding to inflexion point for the smallest observation of g_s. The average of x_0 and x_i was subsequently used as the initial guess for the Ψ_{ref} parameter upon fitting Equation 7 (i.e., ζ of the main text). The initial guess for s_{TUZ} was always 2.

Ψ_{ref} and s_{TUZ} were calibrated to the upper envelope of non-smoothed normalised observations of g_s to Ψ_l, using the 'optimize.curve_fit' function of the SciPy python package (SciPy 1.0 Contributors et al., 2020). For *Eucalyptus capillosa*, observations of Ψ_l were not available, so Ψ_{ref} was simply set to P_{50} and s_{TUZ} to 2.

Text S7. Performance assessment metrics

The Nash-Sutcliffe Efficiency index (NSE; Nash & Sutcliffe, 1970) is defined as:

$$NSE = 1 - \frac{\sum_{i=1}^{n}(sim-obs)^2}{\sum_{i=1}^{n}(obs-\overline{obs})^2} \quad (7.1)$$

with positive values characterising models more skilled than the observed mean (NSE = 0) and 1 perfect forecasts.

The Mean Absolute Scaled Error (MASE; Hyndman & Koehler, 2006) is:

$$MASE = \frac{\overline{|e_j|}}{\frac{1}{n-1}\sum_{i=2}^{n}|obs_i - obs_{i-1}|} \quad (7.2)$$

where e_j is the forecast error, which we modify to account for the minimum forecast error:

$$e_j = sim - obs - \min_{i\in[n]}(|sim_i - obs_i|) \quad (7.3)$$

A MASE of 0 denotes the minimum possible simulation error and values < 1 identify models more skilled than a one-step forecast of the previous observation.

Finally, the ranked Bayesian Information Criterion (rBIC) is calculated as the quantile rank of each model's BIC within each site × species. Each model's BIC is estimated following Venables & Ripley (2010):

$$BIC = n\ln\left(\frac{\sum_{i=1}^{n}(sim-obs)^2}{n}\right) + k\ln n \quad (7.4)$$

where k is the number of model parameters.

For rBIC, 0 (1) indicates the best (worst) model at trading-off accuracy and complexity (i.e., number of model parameters) within each site × species.

Text S8. Optimisation criteria forms vs. derivative forms

In our implementation of the optimal schemes, we used the optimisation criteria forms (i.e. direct maximisation or minimisation) rather than their commonly used derivative forms. An example derivative form of Equation 11 (i.e., the WUE-f_{Ψ_l} model) would be the following:

$$\frac{\partial A_n}{\partial g_s} - \lambda \frac{\partial E}{\partial g_s} = 0 \qquad (8.1)$$

More examples of derivative forms can be found in e.g., Anderegg et al. (2018), Prentice et al. (2014), or Wang et al. (2020).

We opted to use the optimisation criteria forms because derivative forms can be unstable when optimal schemes are coupled with an energy balance routine (particularly when D_a and PPFD are low) and might therefore require using a high precision solver, which is not desirable considering computing costs.

To illustrate the differences caused by implementation (i.e. optimisation criteria forms vs. derivative forms), Figure S2 shows a diurnal time course of g_s and Ψ_l for five example models, for a 'low' vs. 'high' solving resolution (100,000 vs. 4,800,000 possibilities in the solving matrices at every instant). It is apparent from Figure S2a, c that the optimisation criteria forms (plain lines) are more stable than the derivative forms (dotted lines) when the solving resolution is low, avoiding spurious large 'peaks' in the morning and evening (those even occur in the afternoon for WUE-f_{Ψ_l}).

For most of the models (but not WUE-f_{Ψ_l}), spurious peaks given by the derivative forms disappear when a high solving resolution is used (Figure S2b, d) and both the actual optimisation criteria and derivative forms agree. However, changing the solver resolution changes the magnitude of g_s and Ψ_l predicted by the LeastCost model's derivative form, which suggests it is prone to artefacts and confirms that the actual criterion form should be preferred.

References

Anderegg, W. R. L., Wolf, A., Arango-Velez, A., Choat, B., Chmura, D. J., Jansen, S., et al. (2018). Woody plants optimise stomatal behaviour relative to hydraulic risk. *Ecology Letters*, *21*(7), 968–977. https://doi.org/10.1111/ele.12962

Choat, B., Ball, M. C., Luly, J. G., Donnelly, C. F., & Holtum, J. A. M. (2006). Seasonal patterns of leaf gas exchange and water relations in dry rain forest trees of contrasting leaf phenology. *Tree Physiology*, *26*(5), 657–664. https://doi.org/10.1093/treephys/26.5.657

Collatz, G. J., Ball, J. T., Grivet, C., & Berry, J. A. (1991). Physiological and environmental regulation of stomatal conductance, photosynthesis and transpiration: a model that includes a laminar boundary layer. *Agricultural and Forest Meteorology*, *54*(2–4), 107–136. https://doi.org/10.1016/0168-1923(91)90002-8

De Kauwe, M. G., Yan-Shih Lin, & Medlyn, B. E. (2015). *Fitfarquharmodel: Vcmax One-Point Method*. Zenodo. https://doi.org/10.5281/ZENODO.30954

De Pury, D. G. G., & Farquhar, G. D. (1997). Simple scaling of photosynthesis from leaves to canopies without the errors of big-leaf models. *Plant, Cell and Environment*, *20*(5), 537–557. https://doi.org/10.1111/j.1365-3040.1997.00094.x

Farquhar, G. D., Caemmerer, S. von, & Berry, J. A. (1980). A biochemical model of photosynthetic CO2 assimilation in leaves of C3 species. *Planta*, *149*(1), 78–90. https://doi.org/10.1007/BF00386231

Héroult, A., Lin, Y.-S., Bourne, A., Medlyn, B. E., & Ellsworth, D. S. (2013). Optimal stomatal conductance in relation to photosynthesis in climatically contrasting *Eucalyptus*

species under drought: Stomatal responses of eucalyptus under drought. *Plant, Cell & Environment*, *36*(2), 262–274. https://doi.org/10.1111/j.1365-3040.2012.02570.x

Hyndman, R. J., & Koehler, A. B. (2006). Another look at measures of forecast accuracy. *International Journal of Forecasting*, *22*(4), 679–688. https://doi.org/10.1016/j.ijforecast.2006.03.001

Kirschbaum, M., & Farquhar, G. (1984). Temperature Dependence of Whole-Leaf Photosynthesis in Eucalyptus pauciflora Sieb. Ex Spreng. *Functional Plant Biology*, *11*(6), 519. https://doi.org/10.1071/PP9840519

Lasdon, L., Duarte, A., Glover, F., Laguna, M., & Martí, R. (2010). Adaptive memory programming for constrained global optimization. *Computers & Operations Research*, *37*(8), 1500–1509. https://doi.org/10.1016/j.cor.2009.11.006

Limousin, J.-M., Bickford, C. P., Dickman, L. T., Pangle, R. E., Hudson, P. J., Boutz, A. L., et al. (2013). Regulation and acclimation of leaf gas exchange in a piñon-juniper woodland exposed to three different precipitation regimes: Rainfall manipulation in piñon-juniper woodland. *Plant, Cell & Environment*, *36*(10), 1812–1825. https://doi.org/10.1111/pce.12089

Lu, Y., Duursma, R. A., Farrior, C. E., Medlyn, B. E., & Feng, X. (2020). Optimal stomatal drought response shaped by competition for water and hydraulic risk can explain plant trait covariation. *New Phytologist*, *225*(3), 1206–1217. https://doi.org/10.1111/nph.16207

Martin-StPaul, N. K., Limousin, J.-M., Rodríguez-Calcerrada, J., Ruffault, J., Rambal, S., Letts, M. G., & Misson, L. (2012). Photosynthetic sensitivity to drought varies among populations of Quercus ilex along a rainfall gradient. *Functional Plant Biology*, *39*(1), 25. https://doi.org/10.1071/FP11090

Medlyn, B. E., Dreyer, E., Ellsworth, D., Forstreuter, M., Harley, P. C., Kirschbaum, M. U. F., et al. (2002). Temperature response of parameters of a biochemically based model of photosynthesis. II. A review of experimental data. *Plant, Cell and Environment*, *25*(9), 1167–1179. https://doi.org/10.1046/j.1365-3040.2002.00891.x

Mitchell, P. J., Veneklaas, E., Lambers, H., & Burgess, S. S. O. (2009). Partitioning of evapotranspiration in a semi-arid eucalypt woodland in south-western Australia. *Agricultural and Forest Meteorology*, *149*(1), 25–37. https://doi.org/10.1016/j.agrformet.2008.07.008

Monteith, J. L., & Unsworth, M. H. (1990). *Principles of environmental physics* (2nd ed). London ; New York : New York: E. Arnold ; Distributed in the USA by Routledge, Chapman and Hall.

Nash, J. E., & Sutcliffe, J. V. (1970). River flow forecasting through conceptual models part I — A discussion of principles. *Journal of Hydrology*, *10*(3), 282–290. https://doi.org/10.1016/0022-1694(70)90255-6

Nelder, J. A., & Mead, R. (1965). A Simplex Method for Function Minimization. *The Computer Journal*, *7*(4), 308–313. https://doi.org/10.1093/comjnl/7.4.308

Neufeld, H. S., Grantz, D. A., Meinzer, F. C., Goldstein, G., Crisosto, G. M., & Crisosto, C. (1992). Genotypic Variability in Vulnerability of Leaf Xylem to Cavitation in Water-

Stressed and Well-Irrigated Sugarcane. *Plant Physiology*, *100*(2), 1020–1028. https://doi.org/10.1104/pp.100.2.1020

Powell, M. J. D. (1964). An efficient method for finding the minimum of a function of several variables without calculating derivatives. *The Computer Journal*, *7*(2), 155–162. https://doi.org/10.1093/comjnl/7.2.155

Powell, M. J. D. (1994). A Direct Search Optimization Method That Models the Objective and Constraint Functions by Linear Interpolation. In S. Gomez & J.-P. Hennart (Eds.), *Advances in Optimization and Numerical Analysis* (pp. 51–67). Dordrecht: Springer Netherlands. https://doi.org/10.1007/978-94-015-8330-5_4

Prentice, I. C., Dong, N., Gleason, S. M., Maire, V., & Wright, I. J. (2014). Balancing the costs of carbon gain and water transport: testing a new theoretical framework for plant functional ecology. *Ecology Letters*, *17*(1), 82–91. https://doi.org/10.1111/ele.12211

SciPy 1.0 Contributors, Virtanen, P., Gommers, R., Oliphant, T. E., Haberland, M., Reddy, T., et al. (2020). SciPy 1.0: fundamental algorithms for scientific computing in Python. *Nature Methods*, *17*(3), 261–272. https://doi.org/10.1038/s41592-019-0686-2

Storn, R., & Price, K. (1997). Differential Evolution – A Simple and Efficient Heuristic for global Optimization over Continuous Spaces. *Journal of Global Optimization*, *11*(4), 341–359. https://doi.org/10.1023/A:1008202821328

Venables, W. N., & Ripley, B. D. (2010). *Modern Applied Statistics with S* (4. ed., [Nachdr.]). New York: Springer.

Wales, D. J., & Doye, J. P. K. (1997). Global Optimization by Basin-Hopping and the Lowest Energy Structures of Lennard-Jones Clusters Containing up to 110 Atoms. *The Journal of Physical Chemistry A*, *101*(28), 5111–5116. https://doi.org/10.1021/jp970984n

Wang, Y., Sperry, J. S., Anderegg, W. R. L., Venturas, M. D., & Trugman, A. T. (2020). A theoretical and empirical assessment of stomatal optimization modeling. *New Phytologist*. https://doi.org/10.1111/nph.16572

Wu, J., Serbin, S. P., Ely, K. S., Wolfe, B. T., Dickman, L. T., Grossiord, C., et al. (2020). The response of stomatal conductance to seasonal drought in tropical forests. *Global Change Biology*, *26*(2), 823–839. https://doi.org/10.1111/gcb.14820

Xiang, Y., & Gong, X. G. (2000). Efficiency of generalized simulated annealing. *Physical Review E*, *62*(3), 4473–4476. https://doi.org/10.1103/PhysRevE.62.4473